

# A comparison of digital radiography systems in terms of effective detective quantum efficiency

Marco Bertolini<sup>a)</sup> and Andrea Nitrosi

*Department of Advanced Technology, Medical Physics Unit, Azienda Ospedaliera ASMN, Istituto di Ricovero e Cura a Carattere Scientifico, Reggio Emilia 42123, Italy*

Stefano Rivetti

*Fisica Medica, Ospedale di Sassuolo S.p.A., Modena 41049, Italy*

Nico Lanconelli

*Alma Mater Studiorum, Physics Department, University of Bologna, Bologna 40127, Italy*

Pierpaolo Pattacini

*Department of Diagnostic Imaging, Radiology Unit, Azienda Ospedaliera ASMN, Istituto di Ricovero e Cura a Carattere Scientifico, Reggio Emilia 42123, Italy*

Vladimiro Ginocchi

*Department of Diagnostic Imaging, Radiology Unit, Azienda USL, Reggio Emilia 42122, Italy*

Mauro Iori

*Department of Advanced Technology, Medical Physics Unit, Azienda Ospedaliera ASMN, Istituto di Ricovero e Cura a Carattere Scientifico, Reggio Emilia 42123, Italy*

(Received 6 September 2011; revised 29 March 2012; accepted for publication 2 April 2012; published 18 April 2012)

**Purpose:** The purpose of this study is to compare digital radiography systems using the metric effective detective quantum efficiency (eDQE), which better reflects digital radiography imaging system performance under clinical operating conditions, in comparison with conventional metrics such as modulation transfer function (MTF), normalized noise power spectra (NNPS), and detective quantum efficiency (DQE).

**Methods:** The eDQE was computed by the calculation of the MTF, the NNPS, the phantom attenuation and scatter, and estimation of x-ray flux. The physical characterization of the systems was obtained with the standard beam conditions RQA5 and RQA9, using the PA Chest phantom proposed by AAPM Report # 31 simulating the attenuation and scatter characteristics of the adult human thorax. The MTF (eMTF) was measured by using an edge test placed at the frontal surface of the phantom, the NNPS (eNNPS) was calculated from images of the phantom acquired at three different exposure levels covering the operating range of the system ( $E_0$ , which is the exposure at which a system is normally operated,  $1/3 E_0$ , and  $3 E_0$ ), and scatter measurements were assessed by using a beam-stop technique. The integral of DQE (IDQE) and eDQE (IeDQE) was calculated over the whole spatial frequency range.

**Results:** The eMTF results demonstrate degradation due to magnification and the presence of scattered radiation. The eNNPS was influenced by the grid presence, and in some systems, it contained structured noise. At typical clinical exposure levels, the magnitude of eDQE(0) with respect to DQE(0) at RQA9 beam conditions was 13%, 17%, 16%, 36%, and 24%, respectively, for Carestream DRX-1, Carestream DRX-1C, Carestream Direct View CR975, Philips Digital Diagnost VM, and GE Revolution XR/d. These results were confirmed by the ratio of IeDQE and IDQE in the same conditions.

**Conclusions:** The authors confirm the robustness and reproducibility of the eDQE method. As expected, the DR systems performed better than the CR systems due to their superior signal-to-noise transfer characteristics. The results of this study suggest the eDQE method may provide an opportunity to more accurately assess the clinical performance of digital radiographic imaging systems by accounting for factors such as the presence of scatter, use of an antiscatter grid, and magnification and focal spot blurring effects, which are not reflected in conventional DQE measures.

© 2012 American Association of Physicists in Medicine. [<http://dx.doi.org/10.1118/1.4704500>]

Key words: physical characterization, eDQE, digital radiography

## I. INTRODUCTION

Digital images have been available for more than two decades in the form of detectors based on photostimulated lumi-

nescence (CR) screen cassettes used in lieu of the traditional screen film x-ray cassettes.<sup>1</sup>

A “digital revolution” took place in the early 2000s, with the diffusion of DR systems (or active matrix flat panel

imagers, AMFPI) consisting in a detection layer deposited over an active matrix array (AMA) of thin film transistors. AMFPI are generally classified as direct or indirect, depending on the characteristics of the detection layer. These devices show a higher image quality with respect to most of the computed radiography systems.

Recently, wireless cassette-sized DR detectors have been developed that have the high image quality typical of AMPFI detectors but can also be used like a conventional cassette, i.e., they can be used with an existing table or wall-stand bucky or for tabletop projections.

Many studies<sup>2–12</sup> have reported largely standardized methods to measure the physical performance of imaging systems based on the International Electrotechnical Commission IEC 62220-1 standard.<sup>4</sup> These studies were based on the metric—the detective quantum efficiency (DQE)—which reflects detector efficiency when forming an image using a limited number of x-ray photons, providing an input signal-to-noise ratio (SNR) at a specific exposure level.

While the DQE does give an image quality measure of the detector per unit of exposure, it does not take into account some important effects present in clinical conditions (i.e., scattered radiation, presence of antiscatter grid, magnification effect, and focal blurring due to focal spot size), resulting in a deterioration in the overall image quality. To overcome this limitation, a theoretical formalism<sup>13–17</sup> and experimental calculations<sup>18–20</sup> have been developed and reported in the literature to calculate the effective DQE (eDQE). The eDQE has a formalism conceptually similar to the DQE calculation but scatter fraction (SF), transmission fraction (t), and magnification (m) in the object plane are considered in the final calculation. Samei *et al.*<sup>18</sup> described a practical framework based on this method to globally compare different digital imaging systems.

The aim of this work is to use that framework in order to compare five digital radiography systems: a wireless gadolinium-oxysulphide ( $Gd_2O_2S(Tb)$ ) phosphor-based

system, a wireless un-structured cesium iodine (CsI) phosphor-based DR system, a CR, and two structured CsI DR systems, all installed in our hospitals in clinical environments and with clinical acquisition settings.

## II. MATERIALS AND METHODS

### II.A. Imaging systems tested

The following five imaging systems were included in the study (Table I):

- 1) A DR retrofitted analog x-ray system using a wall-stand bucky “Burgatti Argostat” [Ing. BURGATTI S.p.A., San Lazzaro di Savena (BO), Italy]. We used this imaging system with a wireless DR Carestreamhealth DRX-1 detector based on indirect conversion with a gadolinium-oxysulphide powdered phosphor ( $Gd_2O_2S(Tb)$ ), a-Si:H photodiode and TFT technology. The detector had a 0.139 mm pixel pitch. The imaging system employed a moving grid with a grid density of 40 lines/cm, 150 cm focus, 50  $\mu$ m Pb strips with 0.2 mm Al interspace, and a grid ratio of 10:1 (Gilardoni, Mandello del Lario, Italy). This system will be designated *DRX-1*.
- 2) A DR retrofitted analog x-ray system using a wall-stand bucky “Burgatti Argostat” [Ing. BURGATTI S.p.A., San Lazzaro di Savena (BO), Italy]. We used this imaging system with a wireless DR Carestreamhealth DRX-1C detector based on indirect conversion with pixelated cesium iodine phosphor (CsI(Tl)), a-Si:H photodiode, and TFT technology. The detector had a 0.139 mm pixel pitch. The imaging system employed a moving grid with 40 lines/cm, 150 cm focus, 50  $\mu$ m Pb strips with 0.2 mm Al interspace, and a grid ratio of 10:1 (Gilardoni, Mandello del Lario, Italy). This system will be designated *DRX-1C*.
- 3) A Philips Bucky Diagnost TS x-ray system (Philips Healthcare, Eindhoven, The Netherlands) coupled with a Carestream Direct View CR975 computed radiography system (Carestream, Rochester, NY). A 35 × 43 cm

TABLE I. Technical characteristics of the five systems evaluated.

System	DRX-1	DRX-1C	XR/d	DiDi VM	CR975
Network	Wireless 802.11n			Wired	
Power	Rechargeable battery			Wired	
Conversion phosphor	Powder $Gd_2O_2S:Tb$	Pixelated CsI	Columnar CsI	Columnar CsI	Powder BaFBr:Eu <sup>2+</sup>
Pixel area	35 × 43 cm		41 × 41 cm	43 × 43 cm	35 × 43 cm
Pixel matrix	3072 × 2560		2048 × 2048	3001 × 3001	2048 × 2500
Pixel pitch	139 $\mu$ m		200 $\mu$ m	143 $\mu$ m	168 $\mu$ m
A/D conversion	14-bits		14-bits	14-bits	12-bits
Image preview	Approx. 6 s		Approx. 5 s	Approx. 7 s	Approx. 35 s
X-ray equip.	Burgatti Argostat		GE Revolution XR/d	Philips Digital Diagnost VM	Philips Bucky Diagnost TS
Grid type	Moving		Stationary	Moving	Moving
Grid lines/cm	40 lp/cm		78 lp/cm	36 lp/cm	36 lp/cm
Grid ratio	10:1		13:1	8:1	12:1
Grid focal distance	150 cm		180 cm	140 cm	150 cm

Carestream PQ Screen (Carestream, Rochester, NY) was employed. The CR screen was composed of granular phosphor ( $\text{BaFBr}(\text{Eu}^{2+})$ ) technology, and the CR reader used a 0.168 mm pixel pitch. The wall-stand bucky employed a moving grid with 36 lines/cm, 180 cm focal distance, and a grid ratio of 12:1 (Philips Healthcare, Eindhoven, The Netherlands). This system will be designated *CR975*.

- 4) A Philips Digital Diagnost VM (Philips Healthcare, Eindhoven, The Netherlands) imaging system employing a detector based on indirect conversion using a columnar iodine cesium phosphor (CsI), a-Si:H photodiode, and TFT technology (Triexell Pixium 4600; Triexell, Moirans, France). The detector pixel pitch was 0.143 mm. The wall-stand bucky employed a moving grid with a grid density of 36 lines/cm, a 140 cm focus, and a grid ratio of 8:1 (Philips Healthcare, Eindhoven, The Netherlands). This system will be designated *DiDi VM*.
- 5) A GE Revolution XR/d (GE Healthcare, Milwaukee, WI) imaging system employing a DR detector based on indirect conversion using a columnar cesium iodine phosphor (CsI), a-Si:H photodiode, and TFT technology (GE Healthcare, Milwaukee, WI). The detector pixel pitch was 0.2 mm. The wall-stand bucky employed a grid with a 180 cm focus, a grid density of 78 lp/cm and 29  $\mu\text{m}$  Pb strips with Al interspace, and a grid ratio of 13:1 (Mitaya Manufacturing Co Ltd., Tokyo, Japan). This system will be designated *XR/d*.

## II.B. Physical characterization

The physical characterization was performed for two standard beam conditions: RQA5 and RQA9. The quantitative comparison was based on the calculation of the modulation transfer function (MTF), normalized noise power spectra (NNPS), and DQE, evaluated using the *IEC 62220-1* standard.<sup>4</sup> In addition, the eDQE was evaluated for the five imaging systems studied. For eDQE calculation, all the systems were evaluated under conditions that emulated those of routine clinical chest examinations with a source-to-image distance (SID) of 180 cm.

## II.C. eDQE evaluation

### II.C.1. Phantoms

For eDQE evaluation, the chest phantom described in AAPM Report # 31 and cited in AAPM Report # 61 was used. This phantom consisted of four pieces of clear acrylic ( $30.5 \times 30.5 \times 2.54 \text{ cm}^3$ ), one  $30.5 \times 30.5 \times 1 \text{ mm}^3$  sheet of aluminum (type Al 1100 alloy), one  $30.5 \times 30.5 \times 2.0 \text{ mm}^3$  sheet of aluminum (type Al 1100 alloy), and a 5.08 cm air gap (Fig. 1). This phantom was designed to emulate typical attenuation and scatter conditions encountered during adult chest radiography.

### II.C.2. Noise measurements

Figure 1 shows the phantom setup used to obtain measurements of the effective NNPS (eNNPS) employed in the

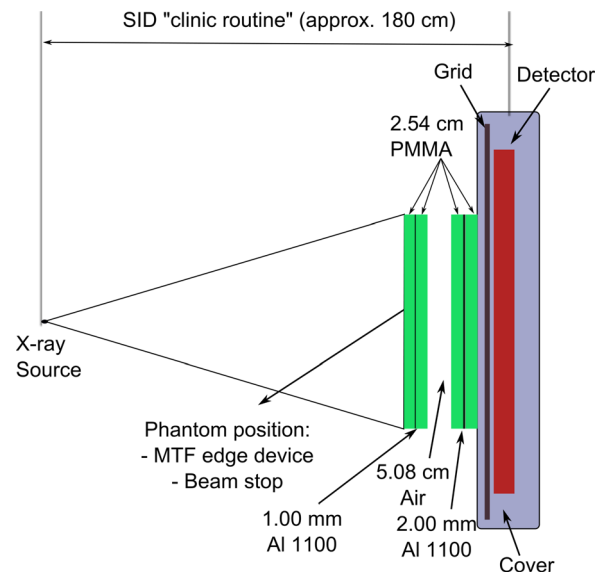


Fig. 1. Phantom setup for the eDQE calculation. The MTF edge device and beam stop device were placed directly in front of the phantom.

computation of eDQE [Eq. (2)]. The phantom was placed at the center of the detector cover plane, and images were obtained without any added filtration. Ten images were acquired using three exposure levels spanning the clinical dose range ( $\sim 1/3 E_0$ ,  $E_0$ , and  $3E_0$ , where  $E_0$  is the “normal” exposure level as specified by the manufacturer for use in clinical practice).

A central ROI of  $20 \times 20 \text{ cm}^2$  was extracted from each image and subdivided into sub-regions of  $128 \times 128$  pixels. The 2D eNNPS was calculated by averaging the squared modulus of the Fourier transform of each subregion. The results were normalized for the square mean signal value of the ROI. Typically, the conventional DQE is measured in the image plane adjacent to the image receptor. However, to evaluate the eDQE relative to the plane of interest in the object, a correction for the magnification associated with

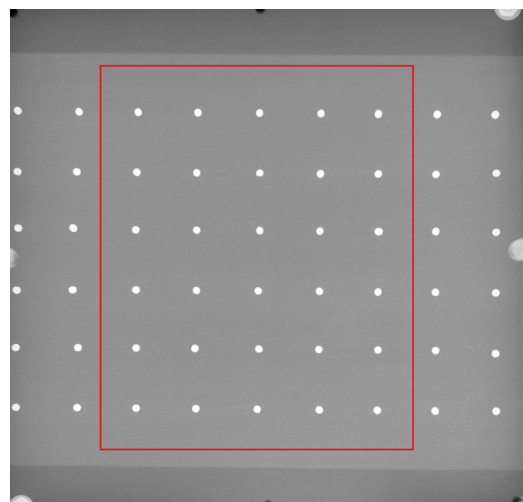


Fig. 2. Radiographic image of the beam stop device. This test object was used to measure the scatter fraction within the central region depicted in the figure (30 lead circular targets).

TABLE II. Specification and characteristics of the exposures used for eDQE calculation (the last column was obtained by multiplying incident exposures by the phantom transmission fractions and the grid transmission fraction).

System	Nominal focal spot size (mm)	kVp	$q$ -value ( $\mu\text{Gy}^{-1} \text{mm}^{-2}$ )	Relationship of pixel value (PV) and air kerma (E in $\mu\text{Gy}$ )	Scatter Fraction (%)	Wide-angle phantom transmission fractions (t)	Incident exposures ( $\mu\text{Gy}$ ) $\sim E_0/3 \sim E_0 \sim 3E_0$	Detector exposures ( $\mu\text{Gy}$ ) $\sim E_0/3 \sim E_0 \sim 3E_0$
DRX-1	1.20	120	29468	PV = 430.54 ln(E) - 313.05 (R2 = 0.999)	41.0	0.058	32.5	0.96
							83.4	2.46
							245.8	7.26
DRX-1C	1.20	120	29468	PV = 444.45 ln(E) - 363.31 (R2 = 0.999)	40.2	0.055	53.2	1.81
							79.6	2.76
							290.7	9.93
CR975	1.20	120	29468	PV = -486.75 ln(E) + 4293.94 (R2 = 0.997)	48.1	0.052	66.8	2.08
							196.0	6.10
							605.2	18.83
DiDi VM	1.20	120	29468	PV = -2.42E+4110.51 (R2 = 1)	49.7	0.057	18.8	0.76
							33.7	1.36
							103.1	4.15
XR/d	1.25	120	29468	PV = 41.47E+8.37 (R2 = 1)	44.5	0.058	21.5	0.71
							66.2	2.18
							211.3	6.97

that plane must be applied. For the purposes of this study, the plane of interest chosen was at the phantom entrance surface, which reflects the worst-case scenario for magnification and focal spot blurring effects

$$f' = mf, \tag{1}$$

$$\text{eNNPS}(f') = \frac{1}{m^2} \text{eNNPS}(f \cdot m), \tag{2}$$

where  $f'$  is the frequency at the phantom plane entrance (worst case possible).

From the 2D eNNPS( $f'$ ), the 1D eNNPS( $f'$ ) was averaged from horizontal and vertical directions (excluding the values along the axes).

**II.C.3. Resolution measurements**

The resolution measurements were taken using the acquisition setup displayed in Fig. 1. The tungsten edge test device

(TX 5; IBA Dosimetry, Schwarzenbruck, Germany) was centered in front of the phantom. For MTF measurements the MTF edge device was placed so that the evaluation edge was oriented with a 2° to 4° offset with respect to the axis of interest, i.e., parallel to or orthogonal to the anode-cathode axis.

Three images per orientation at the higher exposure level (about three times  $E_0$ ) were acquired, and MTF results were averaged. The spatial frequency ( $f$ ) was corrected for the magnification ( $m$ ) effect as shown in Eq. (1). We defined the MTF calculated with this setup as “eMTF.”

**II.C.4. Scatter measurements**

The scatter properties of the five systems were investigated using a beam-stop positioned at the center of the anterior surface of the phantom (Fig. 2).

The beam-stop device was composed of a matrix of 54 lead cylinders (9 cols  $\times$  6 rows), each of which was 3 mm in

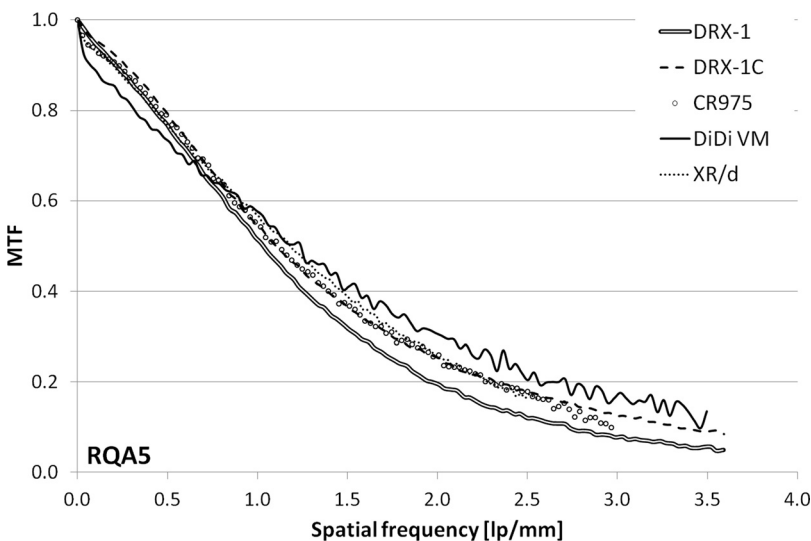


FIG. 3. Presampling MTF curves resulting from the average of the horizontal and vertical directions for each of the five systems for RQA5.

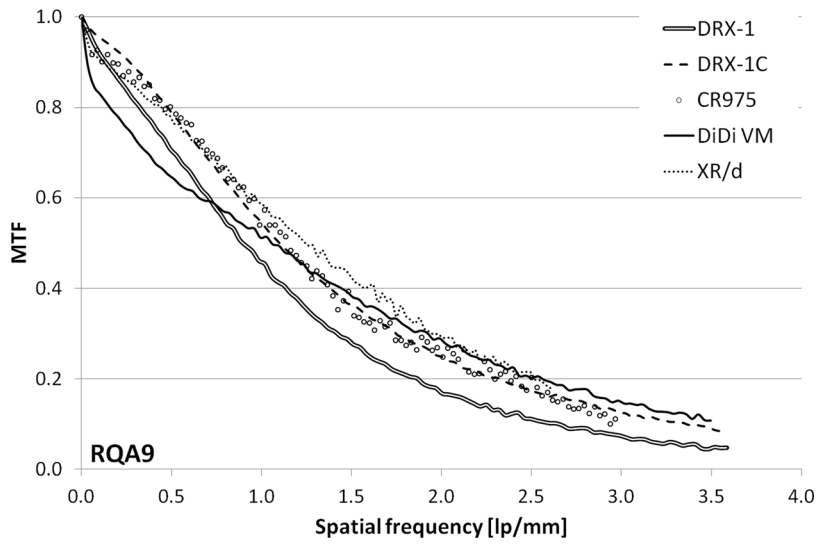


FIG. 4. Presampling MTF curves resulting from the average of the horizontal and vertical directions for each of the five systems for RQA9.

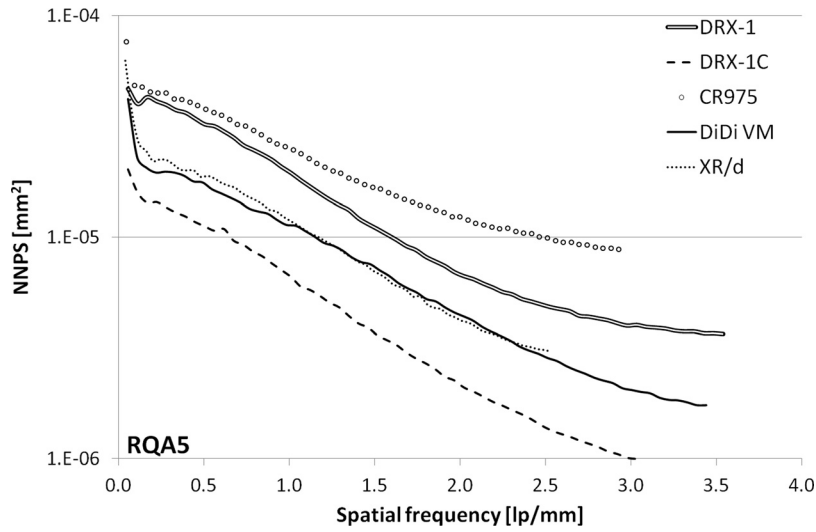


FIG. 5. NNPS curves resulting from the average of the horizontal and vertical directions for each of the five systems for RQA5.

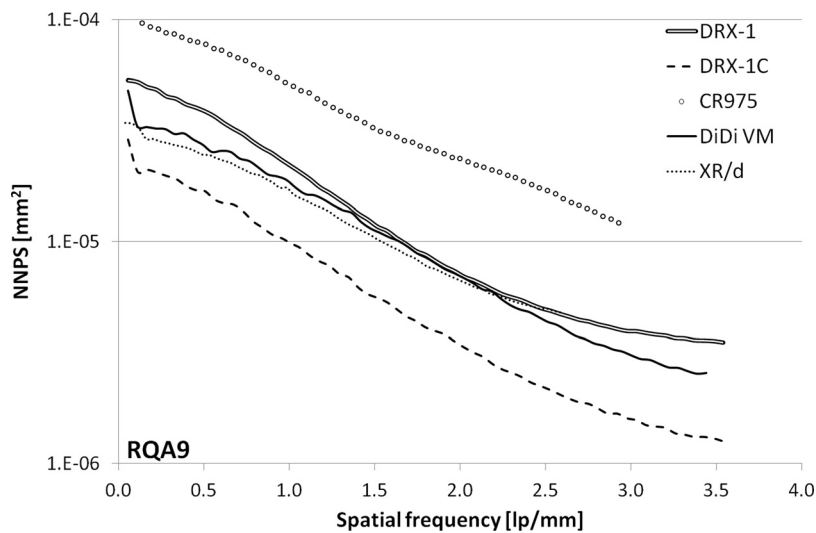


FIG. 6. NNPS curves resulting from the average of the horizontal and vertical directions for each of the five systems for RQA9.

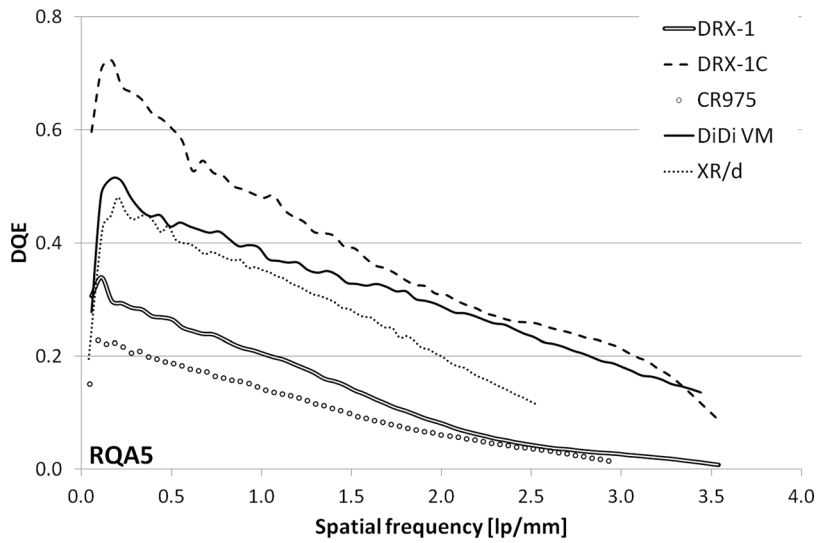


FIG. 7. DQE curves resulting from the average of the horizontal and vertical directions for each of the five systems for RQA5.

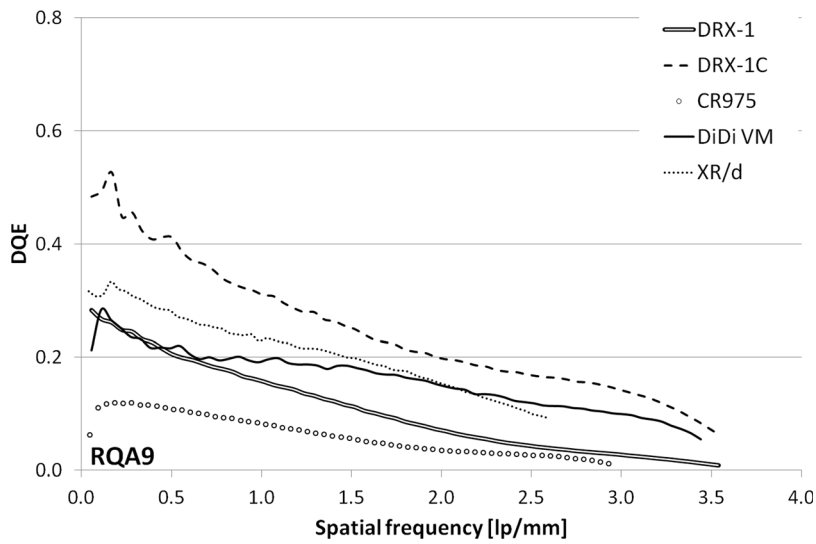


FIG. 8. DQE curves resulting from the average of the horizontal and vertical directions for each of the five systems for RQA9.

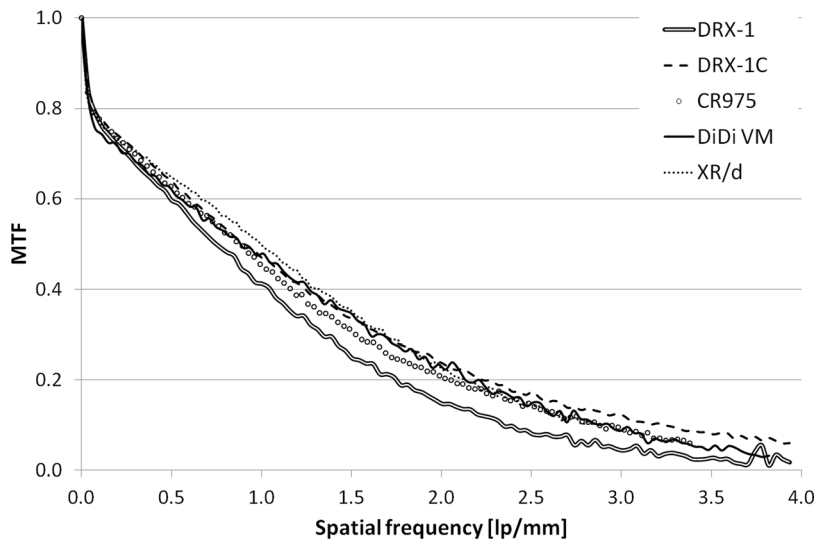


FIG. 9. eMTF curves (resulting from the average of the horizontal and vertical directions) for each of the five systems.

diameter and 6 mm thick, spaced 25 mm apart and embedded in a 6 mm-thick layer of a uniform wood (balsa wood—attenuation less than 2%). Three images were acquired at the highest dose (3E<sub>0</sub>, as for the eMTF measurements).

The average scatter fraction was computed across 30 central beam stops by measuring the mean pixel value in circular regions of interest (ROIs) of 15 pixels in diameter positioned over each beam stop and divided by the average of the mean pixel values on either side of the beam stop.

**II.C.5. eDQE estimation**

The eDQE was then estimated by using the following formula:

$$eDQE(f') = \frac{1}{t} \cdot \frac{eMTF(f')^2 \cdot (1 - SF)^2}{eNNPS(f') \cdot q \cdot E}, \tag{3}$$

where  $f'$  is the spatial frequency corresponding to the object plane of interest (here, the entrance surface of the phantom), which is computed from the spatial frequency in the image plane multiplied by the magnification factor for the object plane of interest. eMTF( $f'$ ) and eNNPS( $f'$ ) are, respectively, the measured eMTF and eNNPS, as described below; SF is the measured scatter fraction,  $E$  is the measured air kerma in  $\mu\text{Gy}$  at the detector plane without the phantom, and  $t$  is the transmission fraction through the phantom using a wide beam geometry. The  $q$  values (ideal photon number per unit of  $\mu\text{Gy}\text{-mm}^2$ ) were

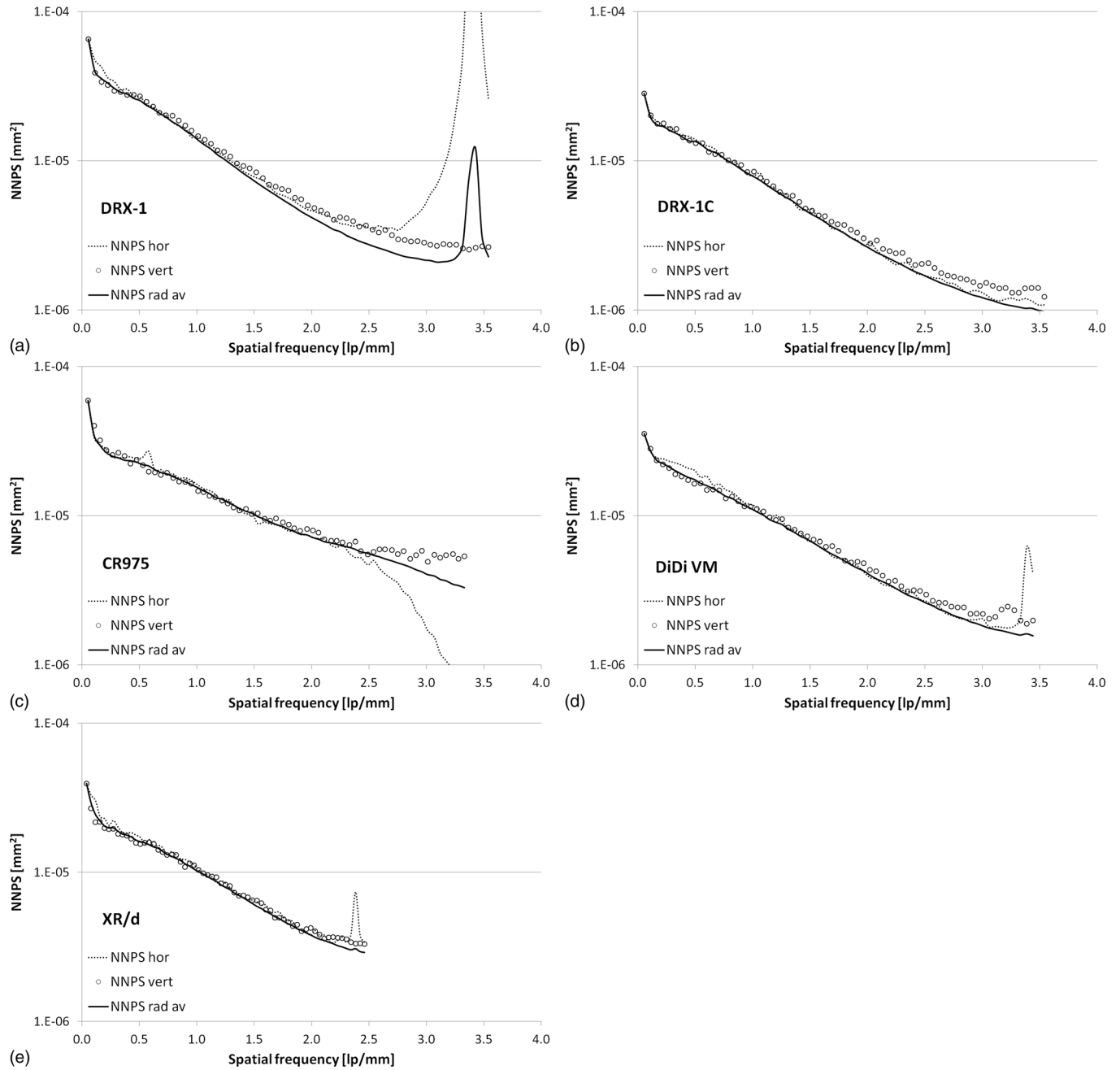


FIG. 10. eNNPS curves (horizontal, vertical, and radial directions) for each of the five systems: (a) DRX-1, (b) DRX-1C, (c) CR975, (d) DiDi VM, and (e) XR/d.

estimated by an x-ray simulation program (xSpect 3.5, Henry Ford Hospital, Detroit, MI) (Ref. 21) assuming an ideal counting detector with an incident primary beam of inherent filtration of 3.5 mm Al, attenuated by the phantom. The measurements were repeated at three exposure levels covering the operating range of the system. The specifications and setup of the systems are summarized in Table II.

### II.C.6. Synthetic image quality index

The integral values of DQE (IDQE) and of eDQE (IeDQE) over the frequency range were adopted as a synthetic image quality index.<sup>5,22</sup> Those quantities were calculated as

$$\text{IDQE} = \int_0^{f_{\text{Nyquist}}} \text{DQE}(f) df, \quad (4)$$

$$\text{IeDQE} = \int_0^{f'_{\text{Nyquist}}} \text{eDQE}(f') df'. \quad (5)$$

The unit of IDQE/IeDQE is  $\text{mm}^{-1}$ . IDQE and IeDQE could be assumed as a reasonable synthetic index of the whole DQE/eDQE curves.

## III. RESULTS

### III.A. Physical characterization (resolution, noise, and DQE at RQA5 and 9)

Figures 3 and 4 show the average of the average horizontal and vertical MTF curves for RQA5 and RQA9 spectra, respectively, for the five systems. Among the CsI-based detectors, the MTF curves for DiDi VM at RQA5 and RQA9 showed the most rapid decrease at low frequencies (low frequency drop).

The DiDi VM detector showed the least degradation of MTF at high frequencies with respect to all other systems. Figures 5 and 6 show the NNPS curves resulting from the average of the horizontal and vertical directions for all five systems evaluated using the RQA5 and RQA9 beam conditions and the normal exposure level ( $\sim 2.5 \mu\text{Gy}$ ). The results obtained using the RQA5 and RQA9 beam conditions showed no significant difference in measurements obtained in the horizontal and vertical directions. The NNPS curves for the two structured CsI detectors are comparable.

Figures 7 and 8 show the DQE curves resulting from the average of the horizontal and vertical directions for each of the five systems for RQA5 and RQA9, respectively, at the operative exposure level (about  $2.5 \mu\text{Gy}$ ). The pixelated phosphor structure of the DRX-1C detector, which minimizes blurring due to light spread in the phosphor layer resulting in a lower noise level, showed the highest DQE of the five systems we evaluated.

#### III.A.1. eMTF, eNNPS, and eDQE

The eMTFs of all systems shown in Fig. 9 demonstrate a low frequency drop at spatial frequencies less than  $0.3 \text{ mm}^{-1}$  due to the presence of scatter, magnification, and focal spot blurring (Fig. 9). DRX-1 presents a lower eMTF than in the other systems (as seen also for MTF).

Both the horizontal and vertical noise results, shown in Figs. 10(a)–10(e), were of the same order of magnitude for all the systems. The eNNPS curves at  $E_0$  exposure level were influenced by the grid presence, visible as a peak in the horizontal direction at spatial frequencies near the Nyquist frequency when corrected for the magnification in the object plane. Figure 11 shows the 2D eNNPS, where the characteristic grid peak near the Nyquist cutoff is clearly visible for all the systems except for DRX-1C.

Figure 12 reports eDQE( $f'$ ) curves for the five systems evaluated. The eDQE(0) performances for all the systems investigated showed a remarkable decrease compared to DQE(0) calculated at RQA 9. The relative ratio between eDQE(0) and DQE(0) was 13%, 17%, 16%, 36%, and 24%, respectively, for DRX-1, DRX-1C, CR975, DiDi VM, and XR/d.

### III.B. IDQE and IeDQE

The IDQE and IeDQE values for different exposure levels are summarized in Table III. The ratio between IeDQE and IDQE, which can be considered an index of overall system optimization, shows that the Philips DiDi VM system yielded the best performance at the reference exposure level (Table IV) but showed an optimization index ratio that was significantly lower at higher exposure levels. However, all other systems demonstrated a performance index ratio that was relatively insensitive to exposure (dose) level.

The absolute values for the ratios between IeDQE and IDQE were similar for the DRX-1C and XR/d systems and were of almost the same magnitude for the DRX-1 and CR975 systems.

The IeDQE/IDQE ratios for DRX-1C, XR/d, DRX-1, and CR975 systems were relatively insensitive to the dose, as previously noted.

## IV. DISCUSSION

### IV.A. Physical characterization (resolution, noise, and DQE at RQA5 and 9)

For the photostimulable phosphor detector, the presampling MTF curves were comparable with the CsI detector

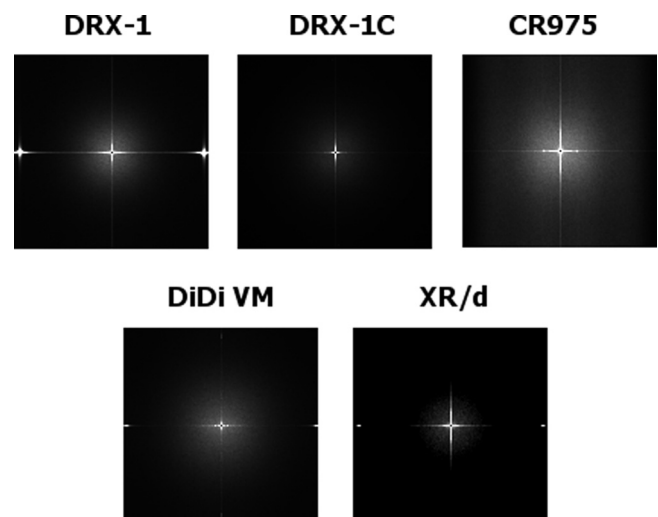


FIG. 11. 2D eNNPS for each of the five systems: (a) DRX-1, (b) DRX-1C, (c) CR975, (d) DiDi VM, and (e) XR/d.



MTF curves. The gadolinium-based detector (granular phosphors) showed the worst MTF, probably due to the directionality of light generation (relatively high fraction of laterally directed optical photons), light absorption, and light scattering. A lower light extinction coefficient (and the resulting light spread) in this type of detector can cause

image quality degradation, depending on the screen characteristics, i.e., thickness, composition, doping, etc.<sup>23</sup>

The pixelated structure of DRX-1C detector, as expected, yielded a lower NNPS and better performance. The rank ordering of the NNPS results for all five systems examined was the same for the RQA5 and RQA9 beam conditions.

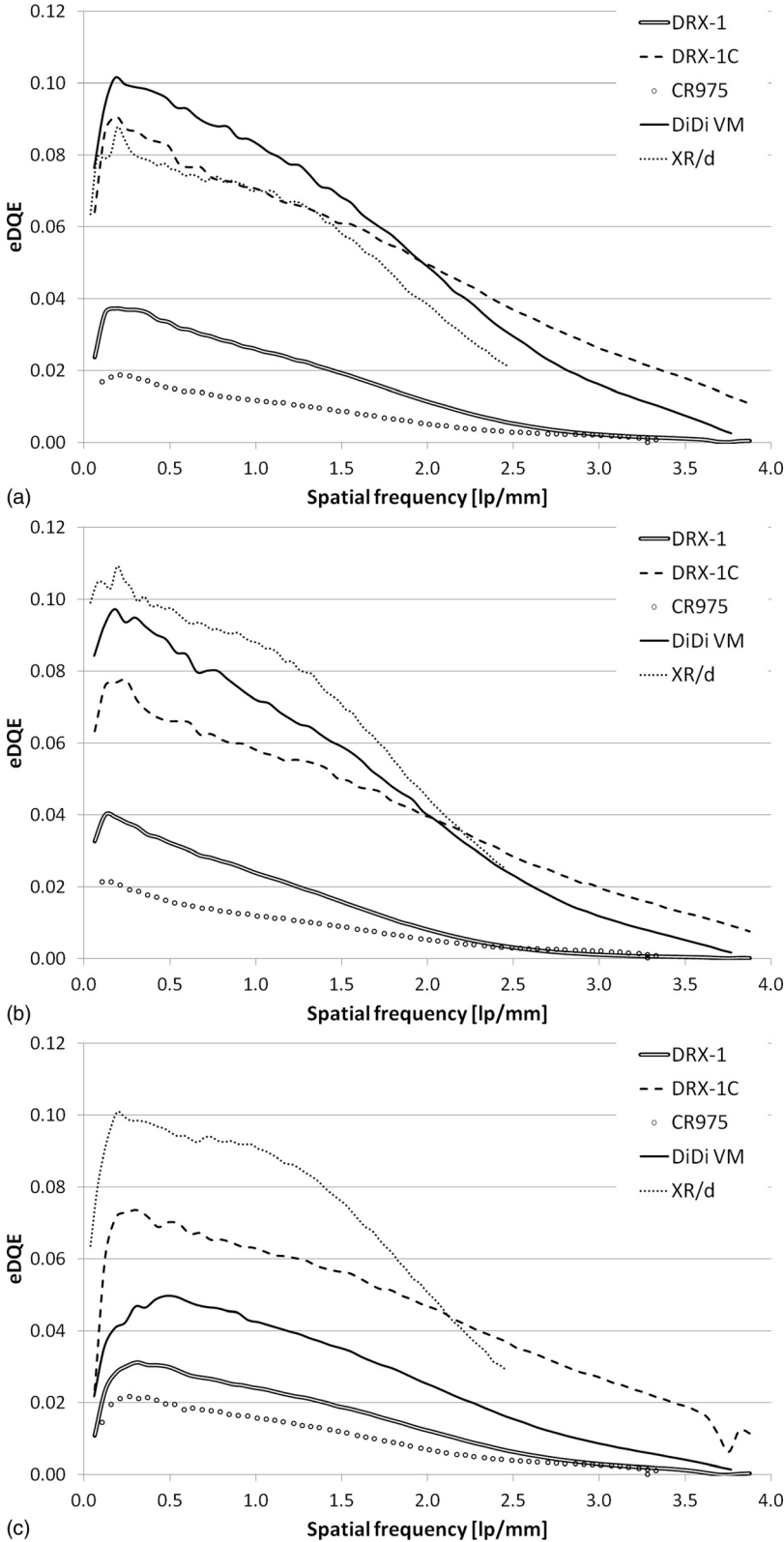


FIG. 12. eDQE curves (resulting from the average of the horizontal and vertical directions) for each of the five systems at the three doses: (a)  $E_0/3$ , (b)  $E_0$ , and (c)  $3 E_0$ .

TABLE III. Comparison between IeDQE (at the three doses considered:  $E_0/3$ ,  $E_0$ , and  $3E_0$ ) and IDQE (at the operative exposure level of about  $2.5 \mu\text{Gy}$ ).

	DRX-1	DRX-1C	CR975	DiDi VM	XR/d
IeDQE @ $E_0/3$ (%)	5.0	16.4	2.3	23.9	13.9
IeDQE @ $E_0$ (%)	5.6	18.9	2.6	19.2	14.4
IeDQE @ $3 E_0$ (%)	5.2	18.2	2.9	13.8	14.2
IDQE (%)	37	86	22	56	74

The gadolinium-based detector NNPS degradation with increasing exposure as the energy increases (RQA9 vs RQA5) was less evident with respect to the other systems. This was probably due to the different K-edge energy and consequent higher fraction of reabsorbed K-fluorescent x-ray photons, which cause a substantial decrease in the x-ray Swank factor.<sup>22</sup>

The gadolinium-based detector DQE degradation as the energy increases was less evident with respect to the other systems, as previously noted. The DiDi VM DQE curves degraded less rapidly with increasing frequency as a result of the observed lower degradation of MTF at high frequencies.

#### IV.A.1. eMTF; eNNPS, eDQE

DRX-1 eMTF was lower than that of other systems (as seen also for MTF). For those systems employing a moving grid, i.e., all those with the exception of the XR/d, the spatially stochastic grid noise was diminished due to spatial averaging of the grid contributing to total noise.

Notably, the only system that did not demonstrate an appreciable peak in noise near the Nyquist frequency when reviewing the NNPS plots was the DRX-1C. In contrast, the DRX-1 showed a well-defined peak both in the 1-D NNPS plot and 2-D NNPS image. The CR975 system demonstrated a small noise peak at frequencies lower than 1 lp/mm likely due to the CR scanner characteristics.

The DRX-1C suffered larger image quality degradation (in terms of eDQE with respect to DQE) for the XR/d and DiDi VM systems. This was probably due to imperfect optimization choice of system components (in particular, the grid type) for the DRX-1C. DiDi VM and XR/d systems are sold as complete systems, while DRX-1, DRX-1C, and CR975 systems can be considered “retrofit” systems.

#### IV.A.2. IDQE and IeDQE

The ratio between IeDQE and IDQE shows that the DiDi VM system is probably the most optimized system at the reference dose of the systems tested. The DiDi VM ratio signifi-

TABLE IV. Ratio between IeDQE and IDQE (for the three doses considered:  $E_0/3$ ,  $E_0$  and  $3E_0$ ) to highlight relative differences as a function of dose.

	DRX-1	DRX-1C	CR975	DiDi VM	XR/d
$E_0/3$ (%)	14	19	11	43	19
$E_0$ (%)	15	22	12	34	20
$3 E_0$ (%)	14	21	13	25	19

cantly changed at higher doses, which might be indicative of a system that would be optimized only for doses near the reference dose or lower, i.e., a dose level near that used when the detector is calibrated.

The DiDi VM degradation of performance (considered in this case as the ratio between IeDQE and IDQE) at high doses (low dose performance appeared worse, albeit slightly, compared to higher doses) was probably an undesired side effect of having the higher performance at the reference dose, a not unexpected result that is consistent with the tradeoffs typically encountered when attempting optimization of any system.

## V. CONCLUSIONS

As previously reported in the literature, the eDQE results were smaller by almost an order of magnitude than conventional DQE results. The eDQE relative performance ranking differed from that obtained using the DQE, demonstrating their difference in performance optimization among the systems evaluated.

The methodology employed in this study has certain limitations. The results were dependent on the specific phantom employed, and therefore, use of a different phantom may yield different results. Specifically, the AAPM clinical chest phantom does not capture the effects of anatomical noise; using of an anthropomorphic phantom that accurately reflects these clinical imaging characteristics would be more useful, albeit much more challenging. In addition, the resolution measurements were performed with the test object at the phantom surface, maximizing the geometric magnification and focal spot blurring. This condition reflects the worst-case scenario, where anatomical structures of interest are positioned more anteriorly, and structures more posteriorly oriented (closer to the detector) are less impacted by these effects. In this study, the effect of image postprocessing was not considered, but when implementing a program of imaging system optimization, this should be evaluated and optimized after all other system aspects have been optimized.

Nevertheless, despite the limitations of our study, our results suggest that the eDQE methodology may be able to guide the clinical technique optimization of a digital radiography system, i.e., the selection of imaging parameter factors such as focal spot size and antiscatter grid characteristics. Further investigation should address their relative effects.

Used in conjunction with other methodologies such as contrast detail analysis or standardized anthropomorphic phantom-based image quality assessment, the eDQE methodology could be applied to assess and quantify the relative performance of digital radiographic imaging systems. However, the evaluation of postprocessing image quality remains an important factor in clinical system performance evaluation and requires attention when attempting to rank the clinical performance of digital radiographic imaging systems.

<sup>a)</sup> Author to whom correspondence should be addressed. Electronic mail: marco.bertolini@asmn.re.it; Telephone: +39 – 0522 – 295813; Fax: +39 – 0522 – 296392.

- <sup>1</sup>International Organization for Standardization, "Photography. Medical radiographic cassettes/screens/films and hard-copy imaging films. Dimensions and specifications," ISO 4090 (ISO, Geneva, 2001).
- <sup>2</sup>E. Samei, N. T. Ranger, J. T. Dobbins III, and Y. Chen, "Intercomparison of methods for image quality characterization. I. Modulation transfer function," *Med. Phys.* **33**, 1454–1465 (2006).
- <sup>3</sup>A. D. Maidment, M. Albert, P. C. Bunch, I. A. Cunningham, J. T. Dobbins III, R. M. Gagne, R. M. Nishikawa, R. L. Van Metter, and R. F. Wagner, "Standardization of NPS measurements: Interim report of AAPM TG16," *Proc. SPIE* **5030**, 523–532 (2003).
- <sup>4</sup>International Electrotechnical Commission, "Medical electrical equipment—Characteristics of digital X-ray imaging devices - Part 1: Determination of the detective quantum efficiency," IEC 62220-1 (IEC, Geneva, 2003).
- <sup>5</sup>G. Borasi, A. Nitrosi, P. Ferrari, and D. Tassoni, "On site evaluation of three flat panel detectors for digital radiography," *Med. Phys.* **30**, 1719–1731 (2003).
- <sup>6</sup>H. Illers, E. Buhr, and C. Hoeschen, "Measurement of the detective quantum efficiency (DQE) of digital x-ray detectors according to the novel standard IEC 62220-1," *Radiat. Prot. Dosim.* **114**, 39–44 (2005).
- <sup>7</sup>S. Rivetti, N. Lanconelli, R. Campanini, M. Bertolini, G. Borasi, A. Nitrosi, C. Danielli, L. Angelini, and S. Maggi, "Comparison of different commercial FFDM units by means of physical characterization and contrast-detail analysis," *Med. Phys.* **33**, 4198–4209 (2006).
- <sup>8</sup>P. Monnin, D. Gutierrez, S. Bulling, D. Lepori, J. F. Valley, and F. R. Verdun, "Performance comparison of an active matrix flat panel imager, computed radiography system, and a screen-film system at four standard radiation qualities," *Med. Phys.* **32**, 343–350 (2005).
- <sup>9</sup>P. Monnin, D. Gutierrez, S. Bulling, D. Guntern, and E. R. Verdun, "A comparison of the performance of digital mammography systems," *Med. Phys.* **34**, 906–914 (2007).
- <sup>10</sup>G. Borasi, E. Samei, M. Bertolini, A. Nitrosi, and D. Tassoni, "Contrast-detail analysis of three flat panel detectors for digital radiography," *Med. Phys.* **33**, 1707–1719 (2006).
- <sup>11</sup>S. Rivetti, N. Lanconelli, M. Bertolini, and D. Acchiappati, "A new clinical unit for digital radiography based on a thick amorphous Selenium plate: Physical and psychophysical characterization," *Med. Phys.* **38**, 4480–4488 (2011).
- <sup>12</sup>S. Rivetti, N. Lanconelli, M. Bertolini, A. Nitrosi, A. Burani, and D. Acchiappati, "Comparison of different computed radiography systems: Physical characterization and contrast detail analysis," *Med. Phys.* **37**, 440–448 (2010).
- <sup>13</sup>I. S. Kyprianou, S. Rudin, D. R. Bednarek, and K. R. Hoffmann, "Generalizing the MTF and DQE to include x-ray scatter and focal spot unsharpness: Application to a new microangiographic system," *Med. Phys.* **32**, 613–626 (2005).
- <sup>14</sup>I. S. Kyprianou, S. Rudin, D. R. Bednarek, and K. R. Hoffmann, "Study of the generalized MTF and DQE for a new microangiographic system," *Proc. SPIE* **5368**, 349–360 (2004).
- <sup>15</sup>I. S. Kyprianou, A. Ganguly, S. Rudin, D. R. Bednarek, B. D. Gallas, and K. I. Myers, "Efficiency of the human observer compared to an ideal observer based on a generalized NEQ which incorporates scatter and geometric unsharpness: Evaluation with a 2AFC experiment," *Proc. SPIE* **5749**, 251–262 (2005).
- <sup>16</sup>G. K. Yadava, I. S. Kyprianou, S. Rudin, D. R. Bednarek, and K. R. Hoffmann, "Generalized performance evaluation of x-ray image intensifier compared with a microangiographic system," *Proc. SPIE* **5745**, 419–429 (2005).
- <sup>17</sup>C. C. Shaw, X. Liu, M. Lemacks, J. X. Rong, and G. J. Whitman, "Optimization of MTF and DQE in magnification radiography—a theoretical analysis," *Proc. SPIE* **3977**, 467–475 (2000).
- <sup>18</sup>E. Samei, N. T. Ranger, A. Mackenzie, I. D. Honey, J. T. Dobbins III, and C. E. Ravin, "Detector or system? Extending the concept of detective quantum efficiency to characterize the performance of digital radiographic imaging system," *Radiology* **249**, 926–937 (2008).
- <sup>19</sup>E. Samei, N. T. Ranger, A. Mackenzie, I. D. Honey, J. T. Dobbins III, and C. E. Ravin, "Effective DQE (eDQE) and speed of digital radiographic system: An experimental methodology," *Med. Phys.* **36**, 3806–3817 (2009).
- <sup>20</sup>E. Samei, N. T. Ranger, I. D. Honey, J. T. Dobbins III, and C. E. Ravin, "Effective dose efficiency: An application-specific metric of quality and dose for digital radiography," *Phys. Med. Biol.* **56**, 5099–5118 (2011).
- <sup>21</sup>M. J. Flynn and E. Samei, "Experimental comparison of noise and resolution for 2k and 4k storage phosphor radiography systems," *Med. Phys.* **26**, 1612–1623 (1999).
- <sup>22</sup>K. A. Fetterly and N. J. Hangiandreou, "Effects of x-ray spectra on the DQE of a computed radiography system," *Med. Phys.* **28**, 241–249 (2001).
- <sup>23</sup>C. M. Michail, G. P. Fountos, P. F. Liaparinos, N. E. Kalyvas, I. Valais, I. S. Kandarakis, and G. S. Panayiotakis, "Light emission efficiency and imaging performance of Gd<sub>2</sub>O<sub>2</sub>S:Eu powder scintillator under x-ray radiography conditions," *Med. Phys.* **37**, 3694–3703 (2010).